

An exploration of dust formation within WCd systems using an advected scalar dust model

J. W. Eatson^{*}, J. M. Pittard & S. Van Loo

School of Physics and Astronomy, University of Leeds, Woodhouse Lane, Leeds LS2 9JT, UK

Accepted XXX. Received YYY; in original form ZZZ

ABSTRACT

Dust production is one of the more curious phenomena observed in massive binary systems with interacting winds. The high wind temperatures, UV photon flux and violent shocks should destroy any dust grains that condense. However, in some extreme cases dust production yields of approximately 30% of the total mass of the stellar winds have been observed. In order to better understand this phenomenon a parameter space exploration was performed using a series of numerical models of dust producing carbon phase Wolf-Rayet (WCd) systems. These models incorporated a passive scalar dust model simulating dust growth, destruction and radiative cooling. We find that sensible dust yields were produced by these simulations, with significant changes that were not solely due to the changing mass loss rates in the systems. This variability was found to be strongly related to the strength of radiative and Kelvin-Helmholtz (KH) instabilities present. We find that there was a pronounced increase in the dust production rate due to an increased wind velocity shear between the colliding winds, with a high velocity shear inducing KH instabilities and drastically increasing dust yields. We also observe that the dust production rate is dramatically increased in colliding wind system that have a greater wind velocity shear.

Key words: stars: Wolf-Rayet – methods: numerical – binaries: general

1 INTRODUCTION

Binary systems with colliding stellar winds are a fascinating type of system, capable of producing a variety of peculiar phenomena. The shocks produced from this wind interaction creates some of the most luminous persistent stellar-mass x-ray sources in the night sky (Rosslowe & Crowther 2015). Within the wind collision region the available mechanical energy can exceed $10^4 L_{\odot}$, producing shocks with temperatures up to 10^8 K.

In particularly energetic colliding wind binary (CWB) systems, dust has been observed to form. In particular, dust formation occurs around evolved Wolf-Rayet WC sub-type stars that are partnered with an OB type main sequence star (a WR+OB binary). Allen et al. (1972) first attributed IR excess around WC systems to dust in the form of amorphous carbon grains; however, the high wind temperatures and extremely high luminosities around WC systems are such that dust grains would be readily destroyed through sublimation processes. Dust has been observed to form in massive quantities in binary systems (so-called WCd systems), despite an additional highly luminous star and shocks that would quickly destroy these nascent, fragile dust grains. The exact mechanisms of dust formation as well as the evolution of dust within these systems are poorly understood. However dust formation rates can be extremely high, up to $10^{-6} M_{\odot} \text{ yr}^{-1}$, or up to approximately 36% of the total wind by mass in the case of WR104 (Lau et al. 2020).

Within different colliding wind binary systems, dust may form ei-

ther continuously or periodically. The first such observed dust forming system was the episodic dust forming system WR140, first reported by Williams et al. (1990a) who observed a significant and highly variable infrared excess, consistent with emission from dust grains. The dust production rate was later found to vary by a factor of 40 over an orbit of 7.9 yr (van der Hucht et al. 1999; Thomas et al. 2021). Persistent dust forming systems were subsequently discovered, such as WR104 by Tuthill et al. (1999) and WR98a by Monnier et al. (1999), which is used as the prototypical system in this paper. Whilst the exact mechanism for this condition is not currently known, there is a strong correlation between periodicity and eccentricity, with less eccentric systems forming dust continuously, while highly eccentric systems exhibit episodic dust formation (Crowther 2003). Due to this orbital dependency, it is likely that there is an optimal dust forming separation, where dust can form in large quantities. This could be due to factors such as strong post shock cooling, which is highly dependent on the wind speed and orbital separation. Additionally, dust may be protected from the bulk of the stellar radiation due to the extremely large degree of extinction that may occur in the dense post-shock environment of radiative shocks (Cherchneff 2015).

Direct observation of dust forming CWBs and in particular the wind collision region (WCR) is exceptionally difficult for a number of reasons:

- WR+OB CWB systems are extremely rare. Of the 667 catalogued WR stars at time of writing, 106 have been confirmed to be in a binary system (Rosslowe & Crowther 2015; Williams 2019).
- A WC star is required for dust formation. No nitrogen sub-type Wolf-Rayet (WN) have been observed to form dust.

^{*} E-mail: py13je@leeds.ac.uk

- Not all WC+OB systems are dust producing, limiting the sample size further.
- 56 dust forming systems with a known spectral type have been observed overall. Despite producing an extremely large quantity of dust in their local region, they are outnumbered by AGB stars by ~ 3 orders of magnitude (Ishihara et al. 2011).
- Galactic CWB systems are comparatively distant from earth. For instance, WR 104, a well-studied system, is ~ 2.5 kpc distant (Soullain et al. 2018) and no WCd systems have been detected at a distance of < 1 kpc (Rosslowe & Crowther 2015). This prevents observations of these systems at a high angular resolution.
- Grain growth from small nucleation grains is predicted to be very rapid in CWB systems (Zubko 1998). Therefore studying the initial grain evolution would require observational equipment of extremely high angular resolution.

For these reasons, numerical simulations are useful for modelling the growth of dust grains within this unresolved region. In order to better understand what influences dust production in a CWB system, a parameter space exploration of the wind and orbital parameters was performed. In particular the orbital separation, mass-loss rate and wind velocity were modified for both stars in order to influence the wind momentum ratio, η , and the cooling parameter, χ . The wind momentum ratio is defined as:

$$\eta = \frac{\dot{M}_{\text{OB}} v_{\text{OB}}^{\infty}}{\dot{M}_{\text{WR}} v_{\text{WR}}^{\infty}}, \quad (1)$$

where \dot{M} is the mass loss rate of a star and v^{∞} is the terminal velocity of a star's outflow. A low value for η indicates that the winds are extremely imbalanced, with the WR typically dominating the wind dynamics of the system. The wind momentum ratio determines for a given orbital separation, d_{sep} , the distance from each star to the apex of the wind collision. We define the terms r_{WR} and r_{OB} , representing the distance from the WR and OB stars to the WCR:

$$r_{\text{WR}} = \frac{1}{1 + \eta^{1/2}} d_{\text{sep}}, \quad (2a)$$

$$r_{\text{OB}} = \frac{\eta^{1/2}}{1 + \eta^{1/2}} d_{\text{sep}}. \quad (2b)$$

This assumes the winds both accelerate to terminal speed and that there is no radiative inhibition (Stevens & Pollock 1994) or braking (Gayley et al. 1997). In some systems the winds may be so imbalanced that the stronger wind collides directly with the companion star. The half-opening angle of the WCR can be estimated by the formulae:

$$\theta_c \approx 2.1 \left(1 - \frac{\eta^{2/5}}{4} \right) \eta^{-1/3} \quad \text{for } 10^{-4} \leq \eta \leq 1, \quad (3)$$

to a relatively high degree of accuracy (Eichler & Usov 1993; Pittard & Dawson 2018).

The cooling parameter, χ , compares the cooling time to the escape time from the shocked region for a parcel of gas in the immediate post-shock environment. An approximation can be made using the known parameters of a system using the equation:

$$\chi = \frac{t_{\text{cool}}}{t_{\text{esc}}} \approx \frac{v_8^4 d_{12}}{\dot{M}_{-7}}, \quad (4)$$

where v_8 is the wind terminal velocity in units of 10^8 cm s^{-1} , d_{12}

is the distance to the WCR apex in units of 10^{12} cm , and \dot{M}_{-7} is the mass loss rate in units of $10^{-7} \text{ M}_{\odot} \text{ yr}^{-1}$ (Stevens et al. 1992). $\chi \leq 1$ indicates that radiative cooling is very important, while $\chi \gg 1$ indicates that the system is adiabatic. Strong cooling is aided with slow, dense winds and a high metallicity. As such in many systems the post-shock WR flow will rapidly cool from the immediate post-shock temperature of $\sim 10^8 \text{ K}$ to temperatures in the dust formation range, $T \lesssim 10^4 \text{ K}$. A strongly radiating WCR can also be significantly compressed far more as it loses energy. In comparison, an adiabatic WCR is limited to a maximum density increase of a factor of 4 above the pre-shock wind density for $\gamma = 5/3$. The density increase and cool temperatures result in rapid dust growth and protection from the stellar UV radiation in some systems.

For this paper, we aim to explore how dust formation is affected by the orbital and wind parameters of persistent dust forming WR+OB systems. This is performed by running a series of hydrodynamical simulations with an advected scalar dust model. In Section 2 we outline the methodology of our simulations, and how our dust model is implemented. We discuss our model series parameters, and why these parameters were chosen in Section 3. Finally discuss our results and conclude in Sections 4 and 5.

2 METHODOLOGY

Numerical simulations within this paper utilise the Athena++ hydrodynamical code, a highly modular modern fluid dynamics code (Stone et al. 2020). Simulations are generated in 3D and the Euler hydrodynamical equations are solved in the form:

$$\frac{\partial \rho}{\partial t} + \nabla \cdot (\rho \mathbf{u}) = 0, \quad (5a)$$

$$\frac{\partial \rho \mathbf{u}}{\partial t} + \nabla \cdot (\rho \mathbf{u} \mathbf{u} + P) = 0, \quad (5b)$$

$$\frac{\partial \rho \varepsilon}{\partial t} + \nabla \cdot [\mathbf{u} (\rho \varepsilon + P)] = \dot{E}_{\text{cool}}, \quad (5c)$$

where ε is the total specific energy ($\varepsilon = \mathbf{u}^2/2 + e/\rho$), ρ is the mass density, e is the internal energy density, P is the gas pressure, \mathbf{u} is the gas velocity and \dot{E}_{cool} is the energy loss rate per unit volume from the fluid due to gas and dust cooling, which is elaborated on in section 2.1.

Athena++ has been configured to run using a piecewise linear reconstruction method with a 4th order Strong Stability Preserving Runge-Kutta time-integration method (Spiteri & Ruuth 2002). Athena++ was forked from the original repository and additional routines were written for a colliding wind binary scenario. Routines were created to produce a steady outflow from a small spherical region around a set of cartesian co-ordinates as well as a function to move these co-ordinates with each time-step; these were used to simulate stellar wind outflow and orbital motion, respectively. Additionally, Athena++ was further modified to include an advected scalar dust model for simulating dust growth and destruction as well as a photon emission cooling model to approximate cooling for gas and dust particles within the fluid.

Athena++ utilises OpenMPI for parallelism, breaking the simulation into blocks, which are distributed between processors. The block size is variable, but for these simulations a block size of $32 \times 32 \times 8$ was found to be optimal. This meshblock system is also utilised in mesh refinement for increasing effective resolution. As the CWB systems are being simulated in their entirety, a very large volume needs to be simulated, while at the same time the region between

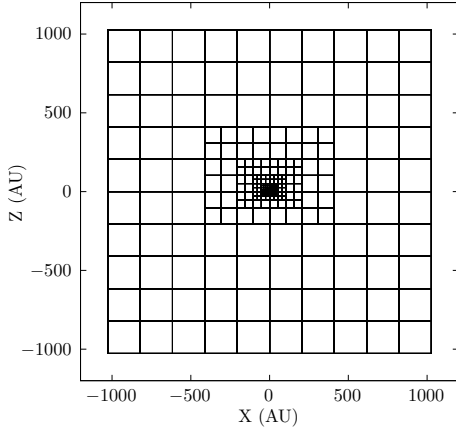


Figure 1. A plot of the blocks used in a 7 level simulation with a block size of $32 \times 32 \times 8$ cells. The block density increases dramatically closer to the barycentre. The coarse simulation resolution is $(320 \times 320 \times 40)$ cells with a block size of $(32 \times 32 \times 8)$ cells. The diagram is sliced about the z axis at $z = 0$.

the stars must be resolved with a resolution of at least 100 cells in order to adequately resolve the WCR. This difference in length scales necessitates the use of static mesh refinement (SMR) to improve the effective resolution of the simulation. A base coarse resolution of $320 \times 320 \times 40$ cells is defined for the simulations, while a region close to the stars operates at a higher refinement level. This results in a resolution increase of a factor of 2^{n-1} greater than the coarse resolution, where n is the refinement level (see Fig. 1). In the case of 7 levels (inclusive of the base, “coarsest” level) as used in most of the simulations in this paper, this results in an effective resolution of $20480 \times 20480 \times 2560$ cells. SMR is utilised instead of Adaptive Mesh Refinement, a more flexible conditional method, as it has proven to be more reliable for our simulations. As much of the grain evolution occurs a small distance from the WCR stagnation point, much of the simulation volume can be run at a lower resolution without affecting the simulation results.

The wind outflow from each star is simulated by replacing the conserved variables (density, momentum and energy) within a small region around the expected position of the stars; this region is typically on the order of 6 maximally refined cells in radius. This rewrite corresponds to a change in density, ρ_R , pressure, P_R , and mechanical energy, E_R , imparted by an outflowing wind, such that

$$\rho_R = \frac{\dot{M}}{(4\pi r^2 v_\infty)}, \quad (6a)$$

$$P_R = \rho_R k_B T_w / \mu m_H, \quad (6b)$$

$$E_R = \frac{P_R}{\gamma - 1} + \frac{1}{2} \rho_R v_\infty^2, \quad (6c)$$

where v_∞ is the wind velocity as it flows radially from the center of the “remap zone”, T_w is the wind temperature and r is the radial distance from the current cell to the centre of the remap zone. Orbits are calculated by moving the remap zones in a manner consistent with Keplerian dynamics, which are repositioned at the start of every timestep. This orbital speed is also added to the remap wind speed.

	X(E)	
	Solar	WC9
H	0.705	0.0
He	0.275	0.546
C	3.07×10^{-3}	0.4
N	1.11×10^{-3}	0.0
O	9.60×10^{-3}	0.05

Table 1. Abundances used for the OB and WR stars being simulated. Other elements are assumed trace when calculating dust emission (Williams et al. 2015).

2.1 Gas and dust cooling

Cooling due to photon emission from atoms, ions and free electrons, as well as dust particles, is simulated by removing energy from a cell at each timestep. The total energy loss is calculated by integrating the energy loss rates due to gas, plasma and dust cooling using the Euler method; in regions with very rapid cooling sub-stepping is used to improve accuracy, with the number of sub-steps being determined by comparing the timestep to the cooling timescale of the cell. Gas cooling is simulated using a lookup table method. A data file containing the gas temperature and associated normalised emissivity, $\Lambda_w(T)$, of the wind at that temperature is read into the simulation. In a typical cooling step, the temperature is calculated and compared with the lookup table to find the closest temperature bins that are lower and higher than the cell temperature. A linear interpolation is then performed to find an appropriate value for $\Lambda_w(T)$. The energy loss in the stellar wind can then be calculated with the formulae:

$$\frac{dE}{dt} = \left(\frac{\rho}{m_H} \right)^2 \Lambda_w(T), \quad (7)$$

where ρ is the gas density and m_H is the mass of a hydrogen atom. The lookup table was generated by mixing a series of cooling curves generated by MEKAL simulations of elemental gasses. These simulations were combined based on the elemental abundances of each wind, with the WC star having typical WC9 abundances and the OB star having a solar abundance (see Table 1). Figure 2 shows the resulting cooling curves used for each star. The most significant abundances used in this projects simulations are presented in Table 1. The cooling regime of the simulations ranges between temperatures of 10^4 to 10^9 K. A floor temperature of 10^4 K is implemented. Temperatures between 1×10^4 K $< T \leq 1.1 \times 10^4$ K is reduced to 10^4 K as they are assumed to be either rapidly cooling or a part of the stellar wind.

A model for cooling due to emission from dust grains is also included as dust cooling was expected to play a significant role in each system. The rate of cooling is calculated using the uncharged grain case of the Dwek & Werner (1981) prescription. Grains are heated due to collisions with ions and electrons, causing them to radiate, with energy being removed from the simulation. This assumes that the region being simulated is optically thin to far infrared photons. The grain heating rate is calculated with the following formulae:

$$H = 1.26 \times 10^{-19} \frac{n}{A^{1/2}} a^2 (\mu m) T^{3/2} h(a, T), \quad (8)$$

where H is the heating rate due to atom and ion collisions, n is the particle number density, A is the mass of the incident particle in AMU, $a(\mu m)$ is the grain radius in microns, T is the temperature of the ambient gas, and $h(a, T)$ is the effective grain “heating factor”, also referred to as the grain transparency.

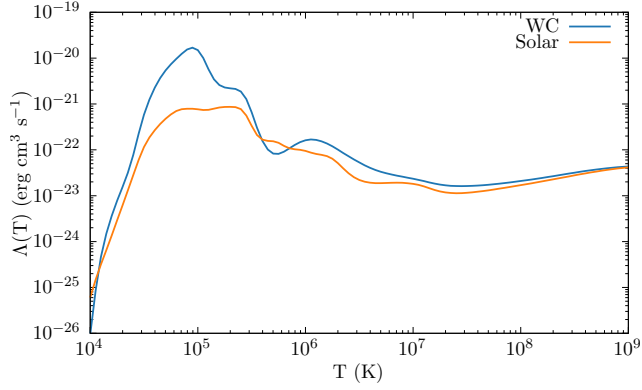


Figure 2. Comparison of WC and solar cooling curves for calculating the energy loss due to gas cooling.

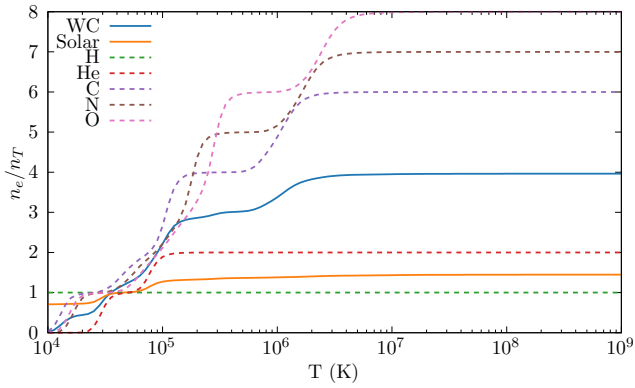


Figure 3. A comparison of the electron-ion ratio in both winds as a function of temperature. Also shown are the electron-to-ion ratios for the individual elements.

To obtain the collisional heating due to incident atoms, H_{coll} , the heating rates are summated for hydrogen, helium, carbon, nitrogen and oxygen atom collisions are summated together:

$$H_{\text{coll}} = H_{\text{H}} + H_{\text{He}} + H_{\text{C}} + H_{\text{N}} + H_{\text{O}}. \quad (9)$$

Other elements are not considered as they are present in trivial proportions in both winds. As dust grains are assumed to be uncharged, the grain transparency for each species is calculated with the formulae:

$$h(a, T) = 1 - \left(1 + \frac{E_0}{2k_{\text{B}}T}\right) e^{-E_0/k_{\text{B}}T}, \quad (10)$$

where E_0 is the initial energy required to overcome the grain's potential and k_{B} is the Boltzmann constant.

Electron-grain collisional heating, H_{el} , is modelled using the same calculation for H_{coll} , albeit with some differences. One major factor for accurately calculating the energy loss due to electron collisions is that the electron number density, n_e , needs to be correct. This is achieved with a second series of lookup tables that contain the electron-to-ion ratio of each wind across a temperature range of 10^4 to 10^9 K (Fig. 3). The electron number density is $n_e = \beta n_i$, where β is the electron-to-ion ratio and n_i is the ion number density. Another difference between calculating electron-grain and gas-grain cooling

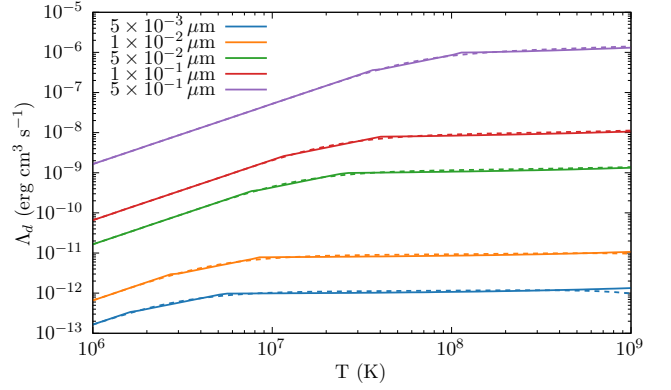


Figure 4. Dust grain cooling curves, $\Lambda_d(T, a)$, as a function of temperature for various grain sizes. The estimate method (Eq. 12, dashed line) is extremely close to the integral value (solid line) aside from at the highest temperatures.

is calculating electron-grain transparency, which is a significantly more complex problem than calculating ion-grain transparency. An assumed full opacity proves to be extremely inaccurate at temperatures $> 10^6$ K. Electron-grain transparency is therefore calculated via an approximation described in Dwek & Werner (1981):

$$\begin{aligned} h(x^*) &= 1, & x^* &> 4.5, \\ &= 0.37x^{*0.62}, & x^* &> 1.5, \\ &= 0.27x^{*1.50}, & \text{otherwise,} \end{aligned} \quad (11)$$

where $x^* = 2.71 \times 10^8 a^{2/3} (\mu\text{m})/T$. This approximation is approximately 4 orders of magnitude faster than using an integration method, while only differing by less than 8% (Fig. 4). Grain-grain collisions are not modelled, as this would be difficult to calculate due to the single-fluid model in use. Further simulations utilising a multi-fluid model could allow for this to be simulated. Finally, in order to calculate the change in energy due to dust cooling, the rate of energy change, dE/dt is calculated using the formulae:

$$\Lambda_d(T, a) = \frac{H_{\text{coll}} + H_{\text{el}}}{n_{\text{H}}}, \quad (12a)$$

$$\frac{dE}{dt} = n_{\text{T}} n_{\text{d}} \Lambda_d(T, a), \quad (12b)$$

where Λ_d is the normalised dust emissivity, n_{H} is the hydrogen number density, n_{T} is the total number density and n_{d} is the dust number density. The total energy loss rate per unit volume due to gas and dust cooling is given by:

$$\frac{dE}{dt} = \left(\frac{\rho}{m_{\text{H}}}\right)^2 \Lambda_{\text{w}}(T) + n_{\text{T}} n_{\text{d}} \Lambda_d(T, a). \quad (13)$$

2.2 Numerical modelling of dust through advected scalars

The most important modification to Athena++ was the addition of a dust growth and destruction model to simulate the production of dust within the WCR. A series of passive scalars were used where the dust parameters described by the scalars can evolve and advect through the simulation, analogous to a co-moving fluid, which previous papers have noted is an accurate dynamical model for dust within the WCR (Hendrix et al. 2016). In these simulations, information about the

dust is stored in the form of two variables, the average grain radius, a , and the dust-to-gas mass ratio, z . From these constants the dust production rate, number density, and total dust mass can be derived. A co-moving model allows for a simplified model of dust formation. In such a model, the mean particle velocity between two particles of different size is:

$$\langle u \rangle = \sqrt{\frac{8kT}{\pi m_r}}, \quad (14)$$

where m_r is the familiar reduced mass between a test particle of mass m_t and a field particle of mass m_f , such that $m_r = m_f m_t / (m_f + m_t)$. As the dust grain is significantly more massive, the reduced mass is approximately equal to the grain mass, simplifying the dynamics of the simulation in a co-moving case.

Dust growth is modelled through approximating growth due to grain-gas accretion where grains co-moving with a gas perform relatively low-velocity collisions with the surrounding gas, causing it to accrete onto the surface of the dust grain (Spitzer 2008). Assuming a single average grain size the rate of change in the average grain radius is given by

$$\frac{da}{dt} = \frac{\xi_a \rho_g w_a}{4\rho_{gr}}, \quad (15)$$

where w_a is the Maxwell-Boltzmann distribution RMS velocity, ξ_a is the grain sticking efficiency, ρ_g is the gas density and ρ_{gr} is the grain bulk density. The associated rate of dust density change is found to be

$$\frac{d\rho_d}{dt} = 4\pi a^2 \rho_g n_d \frac{da}{dt}, \quad (16)$$

where n_d is the grain number density. In this paper we take $\xi_a = 0.1$ as a conservative value, though this value can rise to as high as 1 in the case of highly charged grains. A bulk density analogous to amorphous carbon grains of 3 g cm^{-3} is also used.

Dust destruction is calculated via gas-grain sputtering using the Draine & Salpeter (1979) prescription - a dust grain has a normalised lifespan, τ , which is dependent on the grain radius, and the number density of the gas the grain is moving through, n_g . In the case of spherical amorphous carbon grains, this normalised lifespan is found to be $\tau_d \approx 1 \text{ Myr} \times a/n_g$. The rate of change in grain radius, da/dt , and grain mass, dm_{gr}/dt , as well as the overall dust mass, m_d , and dust density, ρ_d/dt can be calculated with the formulae:

$$\frac{da}{dt} = -\frac{a}{\tau_d}, \quad (17a)$$

$$\frac{dm_{gr}}{dt} = \frac{m_d}{\tau_d} = \frac{4\pi a^3 \rho_{gr}}{3\tau_d}, \quad (17b)$$

$$\frac{d\rho_d}{dt} = \frac{dm}{dt} n_d. \quad (17c)$$

The value for the normalised grain lifespan of $1 \text{ Myr } \mu\text{m cm}^{-3}$ is based on an average lifespan of dust grains in interstellar shocks with shock temperatures between 10^6 and $3 \times 10^8 \text{ K}$ from Dwek et al. (1996), with additional work by Tielens et al. (1994).

Application of the dust growth and destruction routines in the code is determined by the gas temperature of a cell. Dust occurs when $T \leq 1.4 \times 10^4 \text{ K}$ whilst dust destruction occurs at temperatures of $T \geq 10^6 \text{ K}$.

In order to propagate dust through each simulation, a small initial value for the advected scalars is set in each cell in the remap zones.

Parameter	WR	OB
\dot{M}	$5.0 \times 10^{-6} \text{ M}_\odot \text{ yr}^{-1}$	$5.0 \times 10^{-8} \text{ M}_\odot \text{ yr}^{-1}$
v_∞	$1.0 \times 10^8 \text{ cm s}^{-1}$	$2.0 \times 10^8 \text{ cm s}^{-1}$
T_w	$1.0 \times 10^4 \text{ K}$	$1.0 \times 10^4 \text{ K}$

Table 2. Wind properties of the baseline system.

An initial grain radius of $a_i = 50 \text{ \AA}$ and initial dust-to-gas mass ratio of $z_i = 10^{-6}$ is imposed. Changing z_i does not significantly impact the final dust-to-gas mass ratio of the system as z rapidly increases within the WCR and dust growth in the WCR dominates the total production. Dust grows to some extent in the unshocked winds due to this propagation method, however it is extremely low compared to dust production within the shocked winds. A small initial grain radius would also be sensible, as small dust grains are believed to rapidly nucleate from impinging carbon ions (Harries et al. 2004; Zubko 1998).

In order to determine if our dust model is producing sensible dust yields, we calculate the maximum expected dust production rate in each system, $\dot{M}_{d,\text{max}}$. This rate would occur if 100% of the carbon in the WR wind being shocked by the WCR was converted into dust. The fraction of the WR wind that passes through the WCR is given by

$$f_{\text{WR}} = \frac{1 - \cos(\theta_{\text{WR}})}{2}, \quad (18)$$

where θ_{WR} is the opening angle of the WR shock front, approximated as $\theta_{\text{WR}} \approx 2 \tan^{-1}(\eta^{1/3}) + \pi/9$. The theoretical maximum dust production rate is then

$$\dot{M}_{d,\text{max}} = \dot{M}_{\text{WR}} X_{\text{C,WR}} f_{\text{WR}}, \quad (19)$$

where X_{C} is the carbon mass fraction in the WR star (Pittard & Dawson 2018).

3 MODEL PARAMETERS

In this paper we do not attempt to model particular systems. Rather we aim to gain a deeper understanding of the primary influences of dust formation in a CWB system. A series of simulations were therefore run in order to determine how dust formation varies due to changes in orbital separation and wind momentum ratio. A baseline simulation with properties similar to WR98a with a circular orbit and identical stellar masses was created. This baseline simulation has a momentum ratio of 0.02. Other simulations were then run with different orbital separations and/or wind momentum ratios. Another set of simulations were run where the cooling mechanisms were selectively disabled, in order to understand how radiative cooling affects the dust production rate. Tables 2 and 3 detail the wind and orbital parameters of the baseline simulation. The orbital separation is modified by changing the orbital period of the simulation, while the wind momentum ratio is modified by adjusting the mass loss rate and wind terminal velocity for each star. Two simulation sub-sets for this were performed: simulations where the wind terminal velocities were adjusted for each star and simulations where the mass loss rates for each star were adjusted.

3.1 Cooling mechanisms

For this set of simulations, the influence of cooling was changed by varying which cooling routines are operating. All simulations in this

$M_{\text{WR/OB}}$	10.0 M_{\odot}
d_{sep}	4.0 AU
P	1.80 yr

Table 3. Baseline system orbital properties.

Name	Plasma cooling?	Dust cooling?
fullcool	Yes	Yes
plasmacool	Yes	No
nocool	No	No

Table 4. Cooling series simulation parameters.

set keep the same orbital and wind parameters, which are that of the baseline system described in Tables 2 & 3. One simulation has both plasma and dust cooling in operation (the *fullcool* simulation), while the other two simulations have plasma cooling only and no cooling, respectively (*plasmacool* and *nocool*, Table 4). The final, no radiative cooling simulation instead relies on adiabatic expansion for temperature change in the WCR; as such, this simulation behaves as if it has a χ value for both winds that is arbitrarily high. The post-shock flow in the *nocool* model will also be unable to compress as much due to the lack of energy loss via radiative cooling. The role of these simulations is to discern whether cooling alone, or other system parameters can affect dust production.

3.2 Wind momentum ratio

Another set of simulations was devised in order to assess the influence of the wind parameters on the formation of dust within a CWB. As the wind momentum ratio is dependent on both the mass loss rate and wind velocity of each star, each of these properties is modified over a set of different simulations. η is varied from 0.01 to 0.04 by adjusting the wind parameters for each star. This is further subdivided by which property is modified, either the mass loss rate or wind terminal velocity (Table 5). As the cooling parameter, χ , has a much stronger dependency on v_{∞} than \dot{M} , the modification of either parameter while maintaining a similar value for η allows us to determine whether χ is the primary parameter determining the formation of dust within WCd systems. This can be seen when comparing simulations *mdot-1* and *vinf-1*, which have similar wind momentum ratios but the cooling parameters for the WC star differ by a factor of 32. These simulations are compared to the baseline simulation, which has a radiative post-shock WCR. All simulations were run for a minimum of 1 orbit. As these orbits are circular, there should be no major variance of the winds after the start-up transients are fully advected, save for some fluctuations.

3.3 Separation distance

A final series of simulations was performed with the wind parameters equivalent to the baseline model, but with differing orbital separations. The separation was altered by modifying the orbital period, as stellar masses were to be kept realistic. The separation distance was varied from the baseline model of 4 AU up to 64 AU (Table 6), which has the effect of modifying the cooling parameter, χ , of each simulation without changing the wind momentum ratio; allowing us to further discern which is the dominant parameter influencing dust formation. For instance, simulation *dsep-64AU* has a cooling parameter value approaching the fast WR wind model *vinf-1*, despite having a wind momentum ratio of 0.02.

Each simulation has a coarse resolution of $320 \times 320 \times 40$ cells,

with a varying number of levels. As the separation distance is doubled, the associated static mesh refinement box is halved and the number of levels is decremented. This manipulation of levels ensures that the number of cells between the stars is kept consistent and reduces memory usage. The extent for all simulations in this series were doubled over the other series in this paper to approximately $2000 \times 2000 \times 250$ AU. Similarly to the previous set of simulations, a minimum of 1 orbit was needed for each simulation, however, as the orbital period of each simulation varies, certain simulations were able to run for a significantly longer length of time, with data for multiple orbits being obtained.

3.4 Data collection

HDF5 files were generated at regular time intervals - 3D HDF5 meshes were generated every $1/100^{\text{th}}$ of an orbit, while 2D slices were produced every $1/1000^{\text{th}}$ of an orbit. These HDF5 files contain the primitive variables of the simulation: gas density, ρ , gas pressure, P and wind velocity components, v_x , v_y and v_z . These variables were then used to derive other variables such as temperature and energy. The scalars governing the dust properties were also stored for each cell: the dust-to-gas mass ratio, z , and the dust grain radius, a . The wind “colour”, the proportion of gas resultant from each star, was also tracked. A value of 1.0 indicates a pure WR wind while 0.0 indicates a pure OB wind.

The volume-weighted totals of all system parameters were also collected, such as the total gas and dust mass of the system and average grain radius. To derive average values, such as \bar{z} and \bar{a} , from this data, the values for each are divided by the total system mass. To calculate dust formation within the WCR, a method of determining if a cell was part of the wind collision region was devised - the cell density would be compared to the predicted density of a single smooth wind with the wind parameters of the WC star in the system:

$$\rho_{\text{WC}} = \frac{\dot{M}_{\text{WC}}}{4\pi r^2 v_{\text{WC}}^{\infty}}, \quad (20)$$

where r is the distance from the barycentre. This threshold value was set to $1.25\rho_{\text{SW}}$. Higher threshold values were found to be inaccurate at large distances from the barycentre and other methods of detecting the WCR such as determining wind mixing levels, were not successful in general.

4 RESULTS

The first set of simulations were performed in order to assess whether the implemented cooling model would influence dust formation within the WCR. This was found to be the case. Figure 5 shows that with no cooling only a very small amount of dust formation occurs. Dust production in the radiative simulations is significantly higher, with the *fullcool* simulation having consistently higher dust formation rates than the *plasmacool* simulation. This is a sensible result, as Figure 6 shows that at temperatures present within the WCR, dust grains that are present can enhance the cooling, allowing the shocked gas to reach temperatures low enough for dust formation faster than if only plasma cooling was simulated.

In the case of the *fullcool* simulation, a peak dust formation rate of $7 \times 10^{-9} M_{\odot} \text{ yr}^{-1}$ was calculated. This fluctuation appears to be due to dust forming mostly in high density instabilities (see Fig. 5 & 7). The average dust formation rate from these simulations is noted in Table 7. The observed rates are less than 0.1% of the theoretical

Name	\dot{M}_{WR}	\dot{M}_{OB}	v_{WR}^{∞}	v_{OB}^{∞}	η	χ_{WR}	χ_{OB}
baseline	$5.0 \times 10^{-6} M_{\odot} \text{ yr}^{-1}$	$5.0 \times 10^{-8} M_{\odot} \text{ yr}^{-1}$	$1 \times 10^8 \text{ cm s}^{-1}$	$2 \times 10^8 \text{ cm s}^{-1}$	0.02	1.20	1915
mdot-1	$1.0 \times 10^{-5} M_{\odot} \text{ yr}^{-1}$	$5.0 \times 10^{-8} M_{\odot} \text{ yr}^{-1}$	$1 \times 10^8 \text{ cm s}^{-1}$	$2 \times 10^8 \text{ cm s}^{-1}$	0.01	0.60	1915
mdot-2	$2.5 \times 10^{-6} M_{\odot} \text{ yr}^{-1}$	$5.0 \times 10^{-8} M_{\odot} \text{ yr}^{-1}$	$1 \times 10^8 \text{ cm s}^{-1}$	$2 \times 10^8 \text{ cm s}^{-1}$	0.04	2.39	1915
mdot-3	$5.0 \times 10^{-6} M_{\odot} \text{ yr}^{-1}$	$1.0 \times 10^{-7} M_{\odot} \text{ yr}^{-1}$	$1 \times 10^8 \text{ cm s}^{-1}$	$2 \times 10^8 \text{ cm s}^{-1}$	0.04	1.20	957
mdot-4	$5.0 \times 10^{-6} M_{\odot} \text{ yr}^{-1}$	$2.5 \times 10^{-8} M_{\odot} \text{ yr}^{-1}$	$1 \times 10^8 \text{ cm s}^{-1}$	$2 \times 10^8 \text{ cm s}^{-1}$	0.01	1.20	3830
vinf-1	$5.0 \times 10^{-6} M_{\odot} \text{ yr}^{-1}$	$5.0 \times 10^{-8} M_{\odot} \text{ yr}^{-1}$	$2 \times 10^8 \text{ cm s}^{-1}$	$2 \times 10^8 \text{ cm s}^{-1}$	0.01	19.1	1915
vinf-2	$5.0 \times 10^{-6} M_{\odot} \text{ yr}^{-1}$	$5.0 \times 10^{-8} M_{\odot} \text{ yr}^{-1}$	$5 \times 10^7 \text{ cm s}^{-1}$	$2 \times 10^8 \text{ cm s}^{-1}$	0.04	0.07	1915
vinf-3	$5.0 \times 10^{-6} M_{\odot} \text{ yr}^{-1}$	$5.0 \times 10^{-8} M_{\odot} \text{ yr}^{-1}$	$1 \times 10^8 \text{ cm s}^{-1}$	$4 \times 10^8 \text{ cm s}^{-1}$	0.04	1.20	30638
vinf-4	$5.0 \times 10^{-6} M_{\odot} \text{ yr}^{-1}$	$5.0 \times 10^{-8} M_{\odot} \text{ yr}^{-1}$	$1 \times 10^8 \text{ cm s}^{-1}$	$1 \times 10^8 \text{ cm s}^{-1}$	0.01	1.20	120

Table 5. Wind parameters for simulations varying the wind mass loss rate, \dot{M} , and terminal velocity, v^{∞} .

Name	P	d_{sep}	χ_{WR}	χ_{OB}	Levels	Effective Resolution
dsep-4AU	1.80 yr	4 AU	1.20	1915	7	(20480 × 20480 × 2560) cells
dsep-8AU	5.06 yr	8 AU	2.39	3830	6	(10240 × 10240 × 1280) cells
dsep-16AU	14.3 yr	16 AU	4.79	7659	5	(5120 × 5120 × 640) cells
dsep-32AU	40.5 yr	32 AU	9.57	15319	4	(2560 × 2560 × 320) cells
dsep-64AU	115 yr	64 AU	19.1	30638	3	(1280 × 1280 × 160) cells

Table 6. Parameters of simulations varying separation distance.

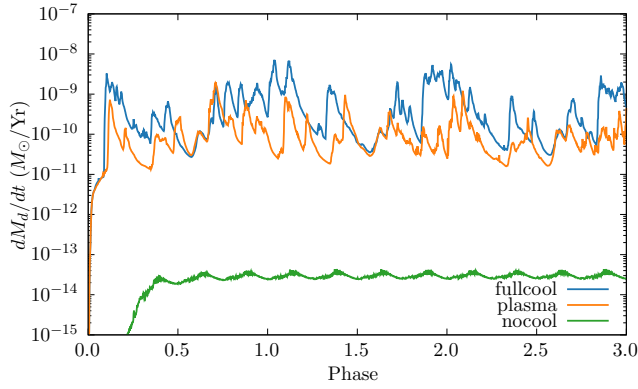


Figure 5. A comparison of dust formation rates as cooling mechanisms are changed. Without adequate cooling barely any dust is formed. While dust formation does increase with all cooling mechanisms enabled, plasma cooling is still the dominant cooling process between 10^4 and 10^9 K for dust production.

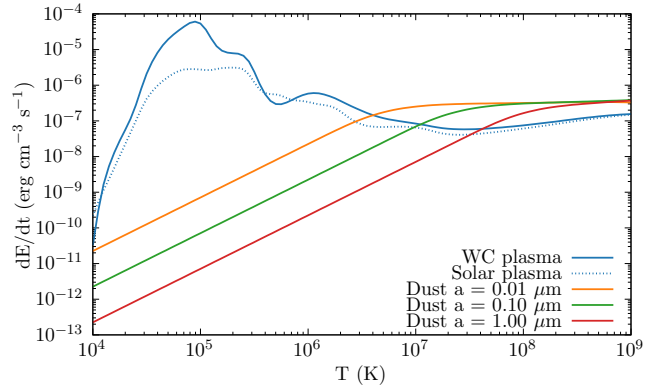


Figure 6. Comparison of the energy loss rate due to plasma and dust cooling with varying grain sizes, where $\rho_g = 10^{-16} \text{ g cm}^{-3}$ (typical of the density in the WCR) and a dust-to-gas mass ratio of 10^{-4} is assumed. Whilst less influential at lower temperatures, dust cooling can aid the overall cooling in the immediate high temperature post-shock environment.

maximum given by Eq. 19, which indicates that even where dust forms the dust-to-gas ratio, z , does not exceed 10^{-3} .

As cooling is significant in the post-shock WR wind ($\chi_{\text{WR}} = 1.2$), further compression occurs, resulting in much higher post-shock densities (Fig. 8). This rapid cooling results in ideal conditions for dust formation, especially within high density instabilities. A similar effect for the OB wind is not observed, as radiative energy losses are not influential on the dynamics of the flow, due to the faster, significantly thinner stellar wind ($\chi_{\text{OB}} = 1915$). Fig. 9 shows that the `fullcool` simulation has a similar immediate-post shock temperature to an adiabatic model, but the shocked WR wind cools to the floor temperature within an extremely short timescale, allowing the nascent dust grains to grow. Fig. 10 shows dust clumps forming shortly after initial wind collision, these clumps rapidly convert post-shock gas to dust; however, rapid dust production tapers off as the post-shock flow becomes more diffuse. This behaviour is similar to previous models, which suggest that the bulk of dust formation occurs only a short distance from the parent stars. The post-shock WCR temperature is significantly lower in the leading edge relative

to the orbital motion, leading to a larger portion of dust forming in this region.

Pittard (2009) notes that in the case of colliding winds with $\eta = 1$ the trailing edge of the WCR takes part in oblique shocks with the stellar winds, while the leading edge is shadowed by the upstream WCR from the colliding material. This results in a trailing edge with strong instabilities and cool, high density clumps of post-shock wind, while the leading edge has a low density flow that is not dominated by instabilities. This does not appear to occur in these low- η systems, as oblique shocks occur at a much greater distance, where the stellar wind is significantly less dense. Instead, the leading edge of the WCR appears to be much thinner and denser than the trailing edge. This is believed to be due to the leading edge interacting more strongly with the outflowing material due to the orbital motion of the stars, sweeping up material and obliquely shocking with the downstream WCR. Most of the dust formation occurs in the downstream post-shock region of the trailing edge of the WCR, as soon as it has sufficiently cooled. Furthermore, dust formation slows significantly as the post-shock wind begins to diffuse, limiting the dust formation

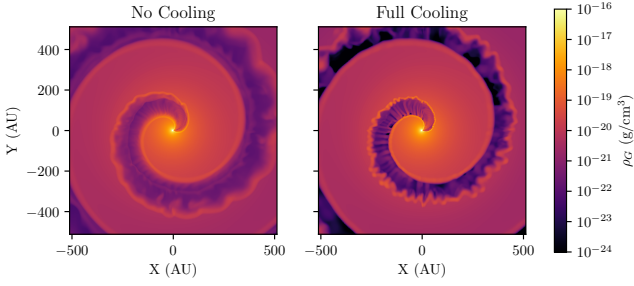


Figure 7. Density comparison in the orbital plane for the *nocool* and *fullcool* models. With cooling enabled instabilities are far more prevalent, with pockets of very high density material within the WCR.

Model	η	χ_{WR}	χ_{OB}	$\dot{M}_{\text{d,avg}}$ $M_{\odot} \text{ yr}^{-1}$	$\dot{M}_{\text{d,max}}$ $M_{\odot} \text{ yr}^{-1}$
<i>fullcool</i>	0.02	1.20	1915	5.38×10^{-10}	9.06×10^{-7}
<i>plasmacool</i>	0.02	1.20	1915	1.29×10^{-10}	9.06×10^{-7}
<i>nocool</i>	0.02	1.20	1915	2.71×10^{-14}	9.06×10^{-7}

Table 7. Average rate of dust production for the set of different radiative simulations. $\dot{M}_{\text{d,max}}$ is the maximum expected dust formation rate (Eq. 19).

Model	η	χ_{WR}	χ_{OB}	$\dot{M}_{\text{d,avg}}$ $M_{\odot} \text{ yr}^{-1}$	$\dot{M}_{\text{d,max}}$ $M_{\odot} \text{ yr}^{-1}$
<i>baseline</i>	0.02	1.20	1915	5.38×10^{-10}	9.06×10^{-7}
<i>mdot-1</i>	0.01	0.60	1915	8.79×10^{-9}	1.42×10^{-6}
<i>mdot-2</i>	0.04	2.39	1915	2.53×10^{-11}	5.83×10^{-7}
<i>mdot-3</i>	0.04	1.20	957	2.34×10^{-8}	1.17×10^{-6}
<i>mdot-4</i>	0.01	1.20	3830	3.81×10^{-11}	7.11×10^{-7}

Table 8. Average rate of dust production for the mass loss rate simulation set.

to a region around 100 AU from the WCR apex. This is in agreement with [Williams et al. \(1990b\)](#) and [Hendrix et al. \(2016\)](#), who found that there is a limited region suitable for dust formation.

4.1 Mass loss rate variation

The dust formation rate in the mass loss variation simulations was found to be dependent on the strength of the WC or OB winds. As can be seen in Fig. 11 and Table 8, the rates are separated into similar dust production rates for simulations with increases or decreases in mass loss rates; simulations with either wind being stronger than the *baseline* simulation produced most dust, while simulations with weaker winds produced approximately 3 orders of magnitude less dust than the most productive simulations. However, the heightened dust production rate does not correspond to the total mass loss rate of the system. For instance, *mdot-1* and *mdot-3* produce on average 2 orders of magnitude more dust with a combined mass loss rate that is 1.99 and 1.01 times higher than the *baseline* simulation. All simulations in this system have low values for χ_{WR} compared to other simulation sets, implying that cooling is not the only governing factor, and that a strong shock must also form.

4.2 Terminal velocity variation

Varying the wind terminal velocity has an extremely strong effect on the dust formation, and is not solely due to cooling (see Fig. 12 and Table 9). The dust production rate is exceptionally high in the case of

vinf-2, which has an extremely slow wind velocity of 500 km s^{-1} , closer to that of a typical LBV star than that of a WC (Table 9). This very slow, dense wind experiences very strong radiative cooling in the post-shock environment ($\chi_{\text{WR}} = 0.07$), driving thermal instabilities and leading to high density pockets of cooled gas. This can be seen in Fig. 13, where *vinf-2* produces large quantities of dust near the apex of the WCR on the WR side, which is then mixed throughout the WCR. This flow is highly radiative and quickly cools back to the initial wind temperature. The factor of 4 difference in the wind velocity between the WR and OB winds creates a strong velocity shear, leading to the formation of Kelvin-Helmholtz instabilities.

It should be noted that the dust production in general increased *outside* of the WCR in the case of *vinf-2* (i.e. in the unshocked WR wind). This is largely due to the significantly higher wind density within the WC wind, and the increase in the time for grain growth before the wind collision. Despite this, the dust production outside of the WCR does not dominate the total dust production rate, most of which occurs in the WCR still. In the numerical analysis of dust production we do not include dust produced outside of the wind collision region. In the case of a fast WC wind, dust production effectively ceases, with an average dust production rate of $9 \times 10^{-14} M_{\odot} \text{ yr}^{-1}$, 2 orders of magnitude less than *vinf-4*, despite having a similar wind momentum ratio.

Simulations *vinf-3* and *vinf-4* show that when the secondary wind velocity is altered, drastic changes to the dust formation rate occur, similar to modifying the mass loss rate of the secondary star. Instabilities due to the secondary wind appear to be the result of this. A greater secondary wind velocity would lead to a greater velocity shear along the discontinuity, resulting in Kelvin-Helmholtz instabilities in *vinf-3* but not in *vinf-4* ([Stevens et al. 1992](#)). Both *vinf-2* and *vinf-3* exhibit KH instabilities, and both have a terminal velocity ratio, $v_{\text{OB}}^{\infty}/v_{\text{WR}}^{\infty} = 4$. This would augment the already present thermal instabilities due to radiative cooling, leading to a less ordered, clumpy post-shock environment. This is found to be the case with *vinf-3*, which has a far greater amount of dust formation within the WCR, and a significantly more mixed wind. In Fig. 14 where *vinf-3* and *vinf-4* are directly compared, the presence of a much faster secondary wind results in a velocity shear that produces a much broader WCR, with high density pockets formed within instabilities, which appear to produce the bulk of dust, despite both simulations having an adiabatic second wind. This suggests that prolific dust formation occurs in a post-shock primary wind shaped by instabilities, produced either from strong radiative cooling, or through a strong velocity shear, leading to K-H instabilities. Radiative cooling is also important beyond thermal instabilities, reducing temperatures in the high-density immediate post shock flow so that dust can begin to form. The results appear to be stratified somewhat in terms of η , simulations where $\eta = 0.04$ produce significantly more dust than simulations with more imbalanced winds (Fig. 12). However, this dependence is different to the mass loss rate simulation subset, and the separation between models in Fig. 11 is less significant.

By directly comparing two prolific dust producing models with $\eta = 0.04$, *vinf-3* and *mdot-3*, we can see that both WCRs are dominated by instabilities. *vinf-3* in particular is more thoroughly mixed (Fig. 15). In particular, it has a much larger trailing edge that produces large quantities of dust (Fig. 16). These simulations produce approximately the same amount of dust, with *vinf-3* also consistently producing dust in the trailing edge of the WCR. From these results it is clear that the dust production rate is increased if there is a highly imbalanced wind velocity (with a slow WC and fast OB wind) as this leads to a post-shock environment governed by thin-shell and Kelvin-Helmholtz instabilities.

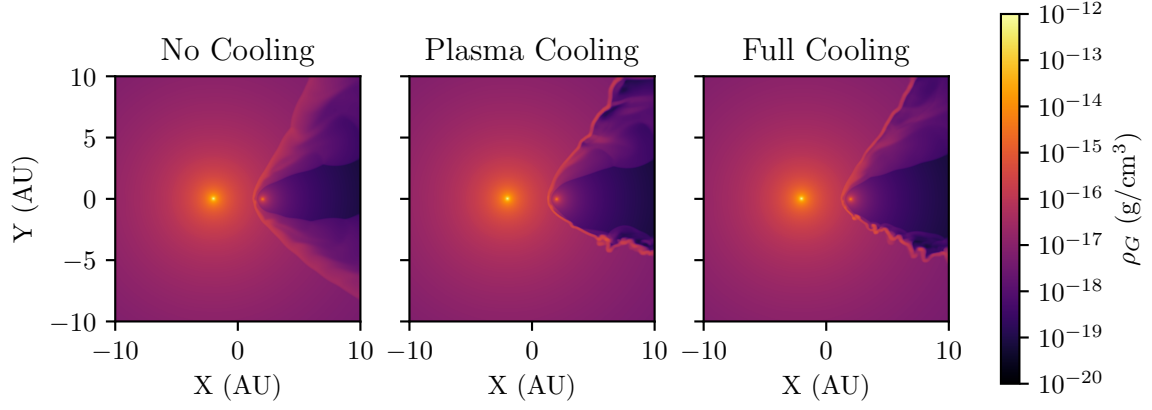


Figure 8. Density comparison in the orbital plane of simulations with differing radiative processes.

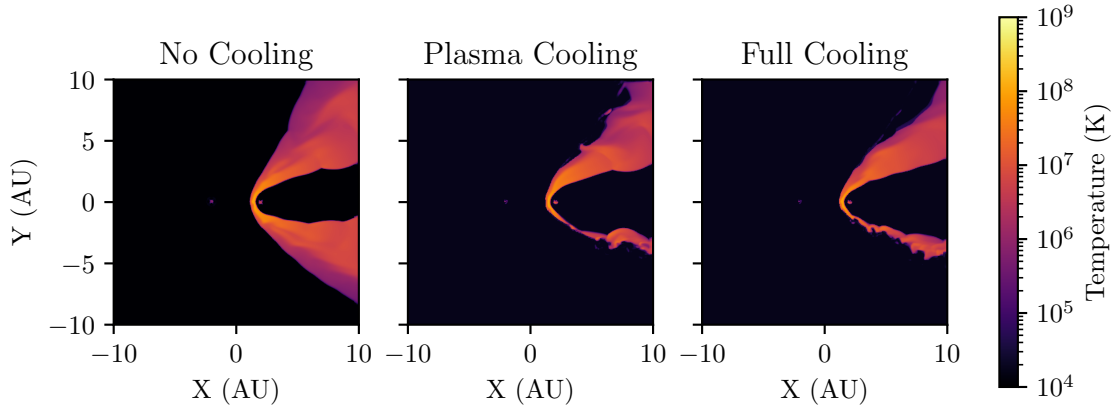


Figure 9. Temperature comparison in the orbital plane of simulations with differing radiative processes.

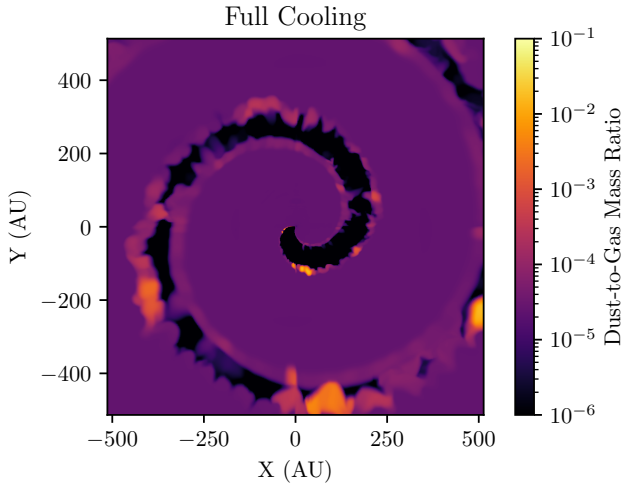


Figure 10. Full extent of baseline simulation, showing the dust-to-gas mass ratio in the orbital plane. Dust typically forms in clumps within instabilities, leading to variation of the dust formation rate as the simulation progresses. Most of the dust forms in the leading arm of the WCR.

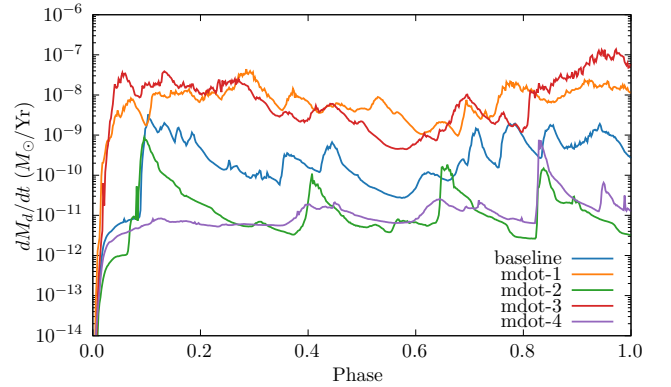


Figure 11. A comparison of the dust production rates for simulations that vary mass loss rate, \dot{M} , simulations with either a strong primary or secondary wind produce similar levels of dust, whilst if either wind is weaker, dust production rate is reduced.

4.3 Separation variation

There is a clear correlation between the separation distance of the stars and the dust formation rate, with dust production drastically increasing as the orbital separation is decreased (Fig. 17 and Table

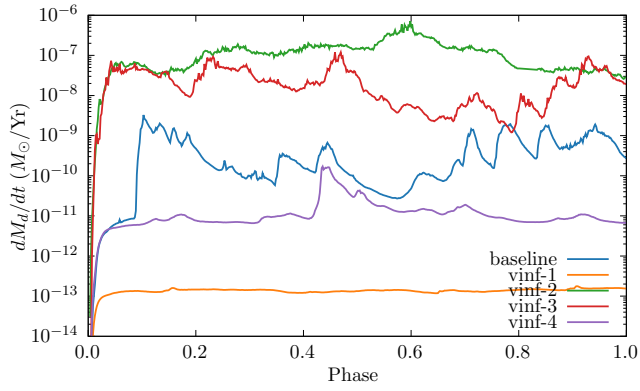


Figure 12. Comparison of the dust production rate for simulations varying the wind terminal velocity, v^∞ . Simulations with a strong wind velocity imbalance produce significantly more dust than their counterparts.

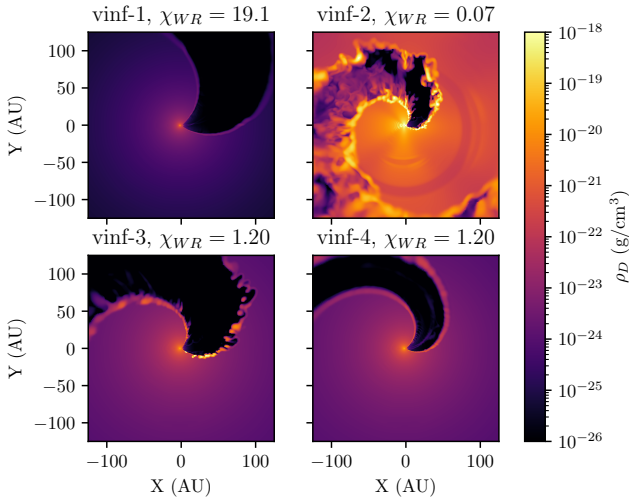


Figure 13. Comparison of the dust density in the simulations that vary v^∞ . Simulations with either a high OB wind velocity or low WC wind velocity produce large quantities of dust. Simulation *vinf-1*, which has a high velocity WC wind, does not produce any appreciable dust within the WCR. *vinf-1* and *vinf-4* have a smoother WCR with less instabilities as both winds have identical terminal speeds, resulting in no velocity shear.

10). This influence on the dust formation rate is non-linear, with a doubling of the separation distance decreasing the dust production rate by approximately one order of magnitude. The variability of the dust production rate also appears to increase as the separation distance is reduced, leading to instances where a simulation may temporarily produce more dust than a simulation with a tighter orbit, such as the case with *dsep-4AU* and *dsep-8AU* at an orbital phase of $0.6 < \Phi < 0.65$. As we have previously discussed, instabilities drive slightly intermittent, but highly efficient dust formation, which would explain these fluctuations (Fig. 18).

Our results are consistent with observations of episodic dust forming systems, where infrared emission due to dust is maximised at or shortly after periastron passage. This also lends further evidence that dust formation rates are not influenced solely by the momentum ratio, as this is kept constant, and instead is strongly influenced by the wind density at collision and the strength of the post-shock cooling.

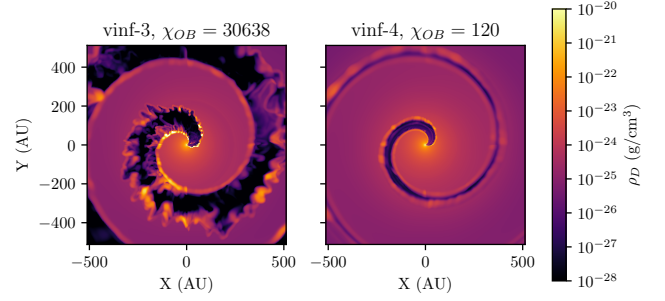


Figure 14. Comparison of the dust density in simulations with modified OB wind terminal velocities. The simulations are fully advected with 3 orbits calculated. Dust formation and instabilities are far more pronounced in *vinf-3*, which has an OB wind velocity a factor of 4 larger than *vinf-4*.

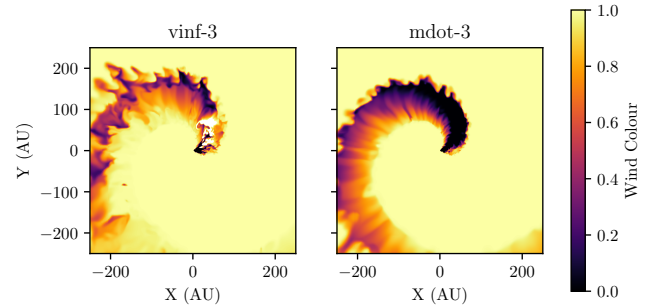


Figure 15. Comparison of the wind colour in simulations *vinf-3* and *mdot-3*. The WR wind has a colour of 1.0 while the OB wind has a colour of 0.0. Wind mixing is significantly more pronounced in *vinf-3* than in *mdot-3*, with a post-shock WR wind that is strongly influenced by Kelvin-Helmholtz instabilities, due to the increased wind velocity imbalance and lower degree of cooling.

Model	η	χ_{WR}	χ_{OB}	$\dot{M}_{d,avg}$ $M_\odot \text{ yr}^{-1}$	$\dot{M}_{d,max}$ $M_\odot \text{ yr}^{-1}$
Baseline	0.02	1.20	1915	5.38×10^{-10}	9.06×10^{-7}
<i>vinf-1</i>	0.01	19.1	1915	8.88×10^{-13}	7.11×10^{-7}
<i>vinf-2</i>	0.04	0.07	1915	1.17×10^{-7}	1.17×10^{-6}
<i>vinf-3</i>	0.04	1.20	30638	6.30×10^{-11}	1.17×10^{-6}
<i>vinf-4</i>	0.01	1.20	120	1.94×10^{-8}	7.11×10^{-7}

Table 9. Average rates of dust production for the terminal velocity simulation set.

5 CONCLUSIONS

The simulations in this paper were conducted over a fairly limited parameter space of mass loss rates and wind terminal velocities. Despite this, the dust production rate varied by up to 6 orders of magnitude. Dust formation was found to be extremely sensitive to the wind properties of both stars, which imposes a limited range of wind parameters for dust to form efficiently. This would explain why these dust forming systems are comparatively rare, compared to the total number of systems with massive binary stars and interacting winds, and also why periodic dust forming systems have eccentric orbits. The baseline system, which is representative of WR98a, has a significantly lower stellar mass loss rate than other well-characterised

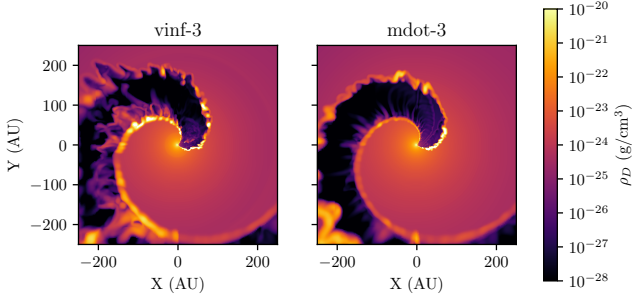


Figure 16. Comparison of the dust density in simulations with a strong secondary wind, *vinf-3* and *mdot-3*. Dust in *vinf-3* is produced to a much higher degree in the trailing edge of the wind rather than on the leading edge of the simulation as in *mdot-3*. The increased mixing of the wind in *vinf-3* due to Kelvin-Helmholtz instabilities has led to dust forming throughout the WCR, rather than being concentrated near the apex of the WCR.

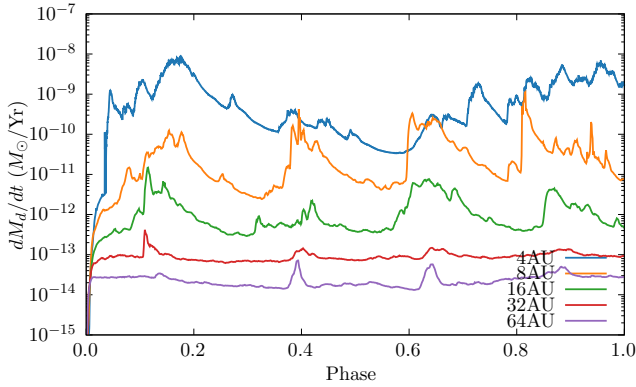


Figure 17. A comparison of dust formation rates versus orbital phase for a set of simulations that vary the separation of the stars, d_{sep} . A clear inverse relationship between separation distance and dust production rate exists, due to a WCR that behaves more adiabatically.

Model	η	χ_{WR}	χ_{OB}	$\dot{M}_{\text{d,avg}}$ $M_{\odot} \text{ yr}^{-1}$	$\dot{M}_{\text{d,max}}$ $M_{\odot} \text{ yr}^{-1}$
dsep-4AU	0.02	1.20	1915	5.38×10^{-10}	9.06×10^{-7}
dsep-8AU	0.01	2.39	3830	4.39×10^{-11}	9.06×10^{-7}
dsep-16AU	0.04	4.79	7659	1.77×10^{-12}	9.06×10^{-7}
dsep-32AU	0.04	9.57	15319	8.83×10^{-14}	9.06×10^{-7}
dsep-64AU	0.01	19.1	30638	2.41×10^{-14}	9.06×10^{-7}

Table 10. Average rates of dust production for the separation distance simulation set.

WCd systems, such as WR140 and WR104. Future simulations will cover these systems to explore how closely they match observations.

5.1 Wind mixing within the WCR

While interaction between hydrogen and dust grains is not simulated by the dust model, elements such as hydrogen are crucial for forming complex organic molecules. As the WC wind is extremely hydrogen-poor, significant wind mixing would need to occur (Herbst & van Dishoeck 2009). Figure 19 shows that the wind is far more effectively mixed by instabilities if it is sufficiently radiative. An improved dust model which can calculate grain yields from chemical reactions could

be used to investigate this further. Conveniently, implementation of a chemical model into Athena++ through passive scalars is a future feature in the projects roadmap. Additionally, a multi-fluid model could be used to model the dynamics of grains, as larger grains may not necessarily be co-moving in a turbulent wind environment.

6 SUMMARY

A parameter space exploration of colliding wind binary systems undergoing dust formation has proven to yield fascinating insights into how dust forms within the WCR. Dust production within these systems is poorly understood, and with direct observations of the WCR rendered difficult by the extreme conditions of these systems, it falls on numerical simulation to elucidate the nature of dust production in CWBs. Most interesting of all is how sensitive to changing wind conditions this dust production is. This parameter space exploration, whilst quite conservative, resulted in a change in dust formation rates of up to 6 orders of magnitude. In all simulations, the bulk of dust formation was found to occur within high-density pockets formed through thin-shell or Kelvin-Helmholtz instabilities, suggesting that strong cooling and a fast secondary wind are both important factors for dust production. For high levels of dust formation, an ideal system should have a slow, dense primary wind and a fast, dense secondary wind, with a close orbit. A combination of these properties ensures the formation of dense pockets of cool post-shock gas ideal for dust formation.

There is significant potential for additional research in this field. Parameter mixing was not performed, due to the simulation time required for producing many more simulations, but performing examples on more extreme systems, such as those with a LBV primary star or a WR+WR system is a potential avenue of research. Future work could introduce additional dust formation and destruction mechanisms, such as grain-grain collision or photodissociation. Modelling effects such as radiative line driving or use of a multi-fluid model could also prove fruitful. Another interesting avenue of research is the simulation of eccentric, periodic dust forming systems; simulating either an entire or a partial orbit of a system such as WR140 would be a logical next step for this work.

7 ACKNOWLEDGEMENTS

This work was undertaken on ARC4, part of the High Performance Computing facilities at the University of Leeds, UK. We would also like to thank P. A. Crowther for his work on the Galactic Wolf-Rayet Catalogue (pacrowther.staff.shef.ac.uk/WRcat).

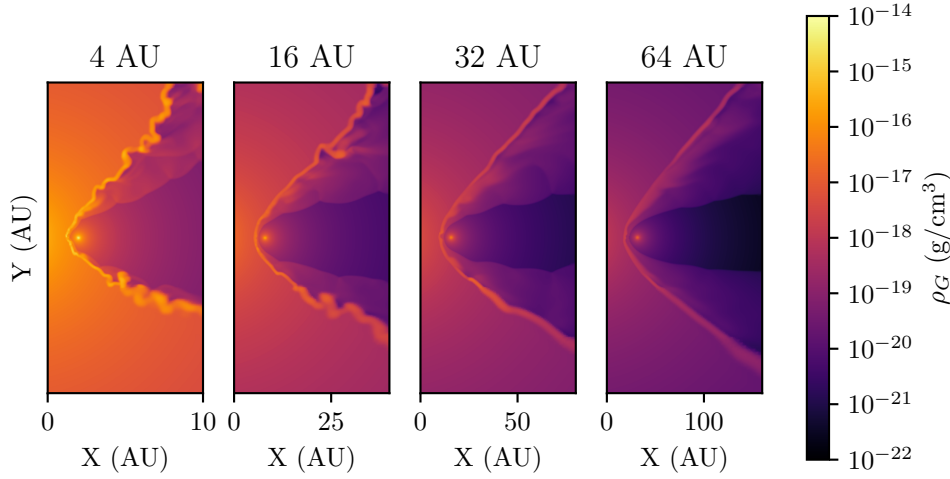


Figure 18. A comparison of the structures of simulations varying d_{sep} . The scale of each plot has been changed to allow for a similar feature size. Simulations with a closer stellar separation have collision regions whose structure is more strongly influenced by instabilities. In particular by thin-shell instabilities brought on by the radiative behaviour in the WCR.

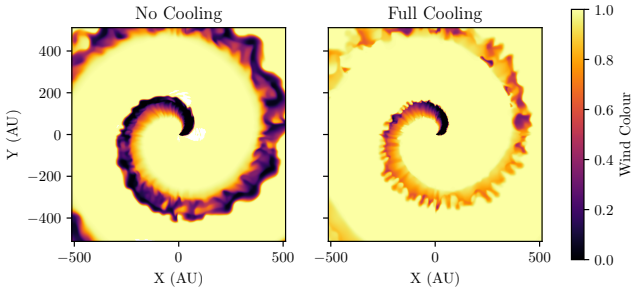


Figure 19. Wind “colour” for nocool and fullcool models. The WCR is more thoroughly mixed if the simulation is allowed to cool.

REFERENCES

- Allen D. A., Swings J. P., Harvey P. M., 1972, *A&A*, 20, 333
 Cherneteff I., 2015, *Dust Formation in Carbon-Rich Wolf-Rayet Colliding Winds*
 Crowther P. A., 2003, *Astrophys. Space Sci.*, 285, 677
 Draine B., Salpeter E., 1979, *ApJ*, 231, 438
 Dwek E., Werner M. W., 1981, *ApJ*, 248, 138
 Dwek E., Foster S. M., Vancura O., 1996, *ApJ*, 457, 244
 Eichler D., Usov V., 1993, *ApJ*, 402, 271
 Gayley K. G., Owocki S. P., Cranmer S. R., 1997, *ApJ*, 475, 786
 Harries T. J., Monnier J. D., Symington N. H., Kurosawa R., 2004, *MNRAS*, 350, 565
 Hendrix T., Keppens R., van Marle A. J., Camps P., Baes M., Meliani Z., 2016, *MNRAS*, 460, 3975
 Herbst E., van Dishoeck E. F., 2009, *ARAA*, 47, 427
 Ishihara D., Kaneda H., Onaka T., Ita Y., Matsuura M., Matsunaga N., 2011, *A&A*, 534, A79
 Lau R. M., Eldridge J. J., Hankins M. J., Lamberts A., Sakon I., Williams P. M., 2020, *ApJ*, 898, 74
 Monnier J. D., Tuthill P. G., Danchi W. C., 1999, *ApJ*, 525, L97
 Pittard J. M., 2009, *MNRAS*, 396, 1743
 Pittard J. M., Dawson B., 2018, *MNRAS*, 477, 5640
 Rosslowe C. K., Crowther P. A., 2015, *MNRAS*, 447, 2322
 Soullain A., et al., 2018, *A&A*, 618, A108
 Spiteri R. J., Ruuth S. J., 2002, *SINUM*, 40, 469

- Spitzer L., 2008, *Physical Processes in the Interstellar Medium*. John Wiley & Sons
 Stevens I. R., Pollock A. M. T., 1994, *MNRAS*, 269, 226
 Stevens I. R., Blondin J. M., Pollock A. M. T., 1992, *ApJ*, 386, 265
 Stone J. M., Tomida K., White C. J., Felker K. G., 2020, *ApJS*, 249, 4
 Thomas J. D., et al., 2021, *MNRAS*, 504, 5221
 Tielens A. G. G. M., McKee C. F., Seab C. G., Hollenbach D. J., 1994, *ApJ*, 431, 321
 Tuthill P. G., Monnier J. D., Danchi W. C., 1999, *Nature*, 398, 487
 Williams P. M., 2019, *MNRAS*, 488, 1282
 Williams P. M., van der Hucht K. A., Pollock A. M. T., 1990a, *MNRAS*, 243, 662
 Williams P. M., van der Hucht K. A., Thé P. S., Bouchet P., 1990b, *MNRAS*, 247, 18P
 Williams P. M., Crowther P. A., van der Hucht K. A., 2015, *MNRAS*, 449, 1834
 Zubko V. G., 1998, *MNRAS*, 295, 109
 van der Hucht K. A., Koenigsberger G., Eenens P. R., 1999, *Wolf-Rayet Phenomena in Massive Stars and Starburst Galaxies*, 193

This paper has been typeset from a \LaTeX file prepared by the author.